Post-subduction tectonics induced by extension from a lithospheric drip

Pilia S.[1,2,3*], Davies D. R.[4], Hall R.[5], Bacon C.[1], Gilligan A.[6], Greenfield T.[1], Tongkul F.[7], Kramer S. C.[8], Wilson C. R.[9], Ghelichkhan S.[4], Cornwell D. G.[6], Colli L.[10], Rawlinson N.[1]

[1] *Department of Earth Sciences-Bullard Labs, University of Cambridge, Cambridge, UK.*

[2] *Department of Earth and Environmental Sciences, University of Milan-Bicocca, Milan, IT.*

[3] *College of Petroleum Engineering and Geosciences, King Fahd University of Petroleum and Minerals, Dhahran, SA.*

[4] *Research School of Earth Sciences, Australian National University, Canberra, AU.*

[5] *SE Asia Research Group, Department of Earth Sciences, Royal Holloway University of London, Surrey, UK.*

[6] *School of Geosciences, University of Aberdeen, Aberdeen, UK.*

[7] *Faculty of Science and Natural Resources, Universiti Malaysia Sabah, Kota Kinabalu, MY.*

[8] *Department of Earth Science and Engineering, Imperial College London, London, UK.*

[9] *Earth and Planets Laboratory, Carnegie Institution for Science, Washington, DC, USA.*

[10] *Department of Earth and Atmospheric Sciences, University of Houston, Houston, USA.*

* Corresponding author (simone.pilia@kfupm.edu.sa)

Subduction termination leads to complex tectonic and geological activity, with the observational record often including clear evidence for exhumation, anomalous magmatism and topographic subsidence, followed by rapid uplift. However, the mechanism(s) driving these responses remain enigmatic and cannot be reconciled with our current understanding of post-subduction tectonics. A prime example of recent subduction termination can be found in northern Borneo (Malaysia), where subduction ceased in the late Miocene (at ~9 Ma). Here, we use recently acquired passive-seismic data to image, at unprecedented resolution (~35 km), a sub-vertical lithospheric drip, inferred to have developed as a Rayleigh-Taylor gravitational instability from the root of a volcanic arc. We use thermo-mechanical simulations to reconcile these images with time-dependent dynamical processes within the crust and underlying mantle following subduction termination. Our model predictions illustrate how significant extension from a lithospheric drip can thin the crust in an adjacent orogenic belt, facilitating lower crustal melting and possible exhumation of subcontinental material, as is observed. These

discoveries provide evidence for extension-driven melting of the lower crust, exhumation, core-complex formation, and orogeny that may also occur in other areas of recent subduction termination.

Introduction:

The segment of continental lithosphere that is now northern Borneo (eastern Malaysia, Fig. 1) bears the signature of two opposing subduction systems that ceased in the Miocene (*1*). Despite ongoing debate (*2-4*) oceanic lithosphere from the Proto-South China Sea (PSCS) is generally thought to have been consumed beneath north-western Borneo between ca 40 and 20 Ma (*2,5,6*). Subduction ended with continental collision of the Dangerous Grounds, which deformed and elevated the Crocker Formation above sea level (Fig. 1). To the northeast, seafloor spreading of the Sulu Sea began at ~21 Ma (*1*), driven by northwest subduction of the Celebes Sea beneath the Sulu arc, as indicated by calc-alkaline volcanism in the Dent and Semporna peninsulas (*7*). Previous work suggests that trench-retreat, driven by slab rollback beneath the Celebes Sea, may have induced significant extension in northern Borneo (*5*), leading to exhumation, accompanied by uplift, of subcontinental peridotite near Ranau and a rift-related magmatic episode (9.2-10.5 Ma) near Telupid (*8*). The slab associated with Celebes Sea subduction is yet to be seismically imaged; however, based on the cessation of arc magmatism, subduction in this area is thought to have terminated at ~9 Ma (*1*). Following subduction termination, a granite pluton was emplaced in a northwest-southeast extensional setting and crystallized between 7.8 and 7.2 Ma (*9,10*), with zircon inheritance patterns implying melting of the underthrust continental crust of the Dangerous Grounds. Thermochronological data from the pluton (*10*) indicate remarkable peak exhumation rates of more than 7 mm/yr from the latest Miocene to the Early Pliocene (~6-4.5 Ma), creating Mt Kinabalu (4095 m elevation), which towers over the Crocker Range (average height 1500 m) and most peaks in southeast Asia. The timing and rate of subsidence and uplift in northern

Borneo remain unresolved, although several lines of evidence suggest Neogene (23 – 2.5 Ma) uplift of 0.3 mm/year for western Sabah (*11*), and subsidence in eastern Sabah (starting at ~14 Ma with widespread sedimentation) followed by rapid uplift, making it fully emergent in the early Pliocene (~5 Ma) (*11,12*). Plio-Pleistocene (~5-2 Ma) intraplate magmatism in the Semporna Peninsula (Fig. 1) indicates a transition from flux-driven volcanism associated with subduction to a system driven by decompression melting (*13*). Relatively recent loading of a fold-and-thrust belt onto the crust of the Dangerous Grounds resulted in a wide flexural depression in the western offshore of Sabah (*5*), a feature that is commonly misinterpreted as the relict PSCS trench location (e.g., *14*). Observations from the mid-late Miocene (~10 Ma) to recent geological record are not easily reconciled with an active subducting system.

Lithospheric foundering in the form of a Rayleigh-Taylor instability (*15*), or 'drip', has been invoked to explain a number of perplexing geological observations across a wide variety of tectonic settings (*16-20*). These drips are rarely detected with seismic imaging due to their relatively small size and rapid descent through the uppermost mantle, but numerical simulations demonstrate an association between downwelling of dense material and topographic subsidence, followed by the removal of lithospheric mantle and topographic uplift (*18,21*). Lithospheric thinning through sinking of gravitational instabilities is also thought to facilitate sub-continental melting (*22,23*): typically, the void created by the missing lower lithosphere is replaced by upwelling asthenospheric mantle, which decompresses, triggering magmatism. Here, we present seismic observations and geodynamic simulations that, when combined with existing geological and geochemical constraints, reveal the central role of such a drip in controlling the post-subduction evolution of northern Borneo.

Results from the nBOSS seismic network

We use data from 46 seismic stations that comprise the temporary northern Borneo Orogeny Seismic Survey (nBOSS) network (Fig. 1, Extended Data Fig. 1), deployed between March 2018 and January 2020. Our dataset is augmented by 28 stations from the national seismic network operated by MetMalaysia. We use analyses of P-to-S receiver functions to determine the thickness of the crust (Methods, Supplementary Information Fig. 1), while relative arrival-time residuals from teleseismic P waves are mapped as 3-D perturbations in the crust and upper mantle (Methods, Extended Data Fig. 2-4, Supplementary Information Fig. 3-4). Anisotropy in the lithospheric mantle is constrained using core-refracted shear phases (Methods, Supplementary Information Fig. 2), and a shear-wave velocity model is used to generate a lithospheric thickness map (Methods).

Receiver-function results document an ~30 km variation in crustal thickness: the regional pattern suggests an alternation of thin and thick crust striking to the NE (Fig. 2A). Surprisingly, the western region of the Crocker Range, including Mt Kinabalu, is underlain by a relatively thin crust (~35 km). Rapid extension at ~10 Ma led to tectonic removal of crustal material and exhumation of the Ranau peridotites (*8*), which include subcontinental lithospheric mantle rocks. If we assume that the region of crustal thickening (50-55 km in Fig. 2A) was produced by continental collision between the Dangerous Grounds and western Sabah, this indicates that the crust beneath the Kinabalu and Ranau area has thinned by about 30%. Another area of even thinner crust (<30 km) is located around Telupid, where recent U-Pb analysis (*8*) found evidence for extension-related magmatism at ~9 Ma (Fig. 1).

The spatial variation of azimuthal anisotropy revealed in our study (Fig. 2C) exhibits two orthogonal orientations that imply two dominant deformational scenarios in the lower lithosphere. The fast orientations of anisotropy in the Crocker Range correlates strongly with the strike of the orogenic belt, suggesting that lattice preferred orientation of uppermost-mantle

minerals may have developed by ductile deformation due to belt-orthogonal compressive stress. Anisotropy orientations near Mt Kinabalu appear to be slightly perturbed from the dominant orogen-parallel pattern in the Crocker Range, and assume a northwest-southeast trend in eastern Sabah. Despite approximate alignment with the direction of absolute plate motion (*24*), it is likely that these orientations are parallel to the back-arc spreading direction created during slab roll-back of the Celebes Sea. Our map of lithospheric thickness, averaging 100 km in the study area, demonstrates that the lower lithosphere is absent beneath the Semporna Peninsula (~40-50 km depth). This is also an area where the splitting analysis returns null observations, which can be explained by vertically oriented flow (Methods, Supplementary Information Fig. 2). Additional direct evidence for thin lithosphere beneath Semporna comes from the estimated melting depth of basalts from sample SBK13 (see Fig. 2D for location), which contains no evidence of contamination from crustal or subduction related processes (*13*). This yielded unusually shallow values of 55±8 km (*25*), implying that intraplate magmatism in Semporna may have been produced by an upper mantle source that likely experienced decompression melting as it upwelled beneath recently thinned lithosphere.

The P-wave tomographic model has several key implications for reconciling the geological and seismic observations with underlying mantle structure and evolution. We image a high-velocity perturbation subparallel to the western coastline of Sabah (Fig. 2B). This anomaly is clearly visible in map view at 300 km depth with a width of ~70 km, consistent with the thickness of the oceanic lithosphere. Most of the PSCS slab is thought to be in the lower mantle (*26*) but we consider a plausible interpretation of this anomaly to be a final upper-mantle remnant of this subducted slab. The vertical section in Fig. 2D indicates that the high-velocity anomaly is a steeply dipping feature; while this suggests that Paleogene subduction could have been at a high angle, it is also plausible that the steep angle was acquired when trench motion became quasi-stationary due to continent-continent collision. This latter process

may have led to slab-detachment at the continent-ocean transition, which can occur even 10 Ma after onset of continental collision (*27*), whilst subsequent plate motion can explain why the PSCS slab is not found further to the east. This result provides important spatio-temporal constraints for unraveling the tectonic history of the PSCS and further refining regional plate motion reconstructions. In addition to the PSCS slab, a vertical profile running from the Semporna Peninsula to Mt Kinabalu (Fig. 2D) in the P-wave tomographic model reveals an elongated high-velocity anomaly extending from ~125-350 km depth, in regions where Extended Data Fig. 3 and 4 suggest minimal vertical smearing. This anomaly does not show lateral continuity (as expected from a slab remnant of the Celebes Sea) and has a dip orientation (tilted from the vertical towards the southeast) broadly consistent with the current direction of absolute plate motion. Significantly, when accounting for an absolute ESE plate motion of ~2.7 cm/yr (*24*), its restored surface location coincides with the region where we inferred vertical flow and lack of lower lithosphere in the Semporna Peninsula (Fig. 2C), pointing towards its initiation at the root of the former volcanic arc, as has been postulated for Rayleigh-Taylor instabilities elsewhere on Earth (*16-18, 28*).

Based upon the joint analysis of our seismic results with the surface geological evidence, we interpret the northwest dipping high-velocity anomaly as a Rayleigh-Taylor gravitational instability that developed from the Dent-Semporna volcanic arc root, which we name the Semporna Drip (SD in Fig. 2D). We hypothesize that such a lithospheric drip can induce widespread extension in areas of thick crust, at distances that extend 100s of kilometers from the locus of the instability, as the lower lithosphere is removed and descends into the asthenospheric mantle. In the context of Sabah, we propose that the SD has thinned the crust of the Crocker Range, facilitating melting of the lower crust and emplacement of Mt Kinabalu. We also postulate that subsidence and uplift in eastern Sabah, in addition to observed intra-

plate volcanism in the Semporna Peninsula (*13*), and possibly Telupid, can be reconciled with the spatial and temporal evolution of the SD.

Dynamic effects of post-subduction lithospheric drip

For simplicity, we perform our numerical simulation in 2-D (Fig. 3, Methods, model setup in Extended Data Fig. 5 and Extended Data Table S1), which allow us to capture the fundamental behavior of this 3-D system. Our simulation provides a dynamical mechanism that explains why a mountain as high as Mt Kinabalu is situated in the Crocker Range, underpinned by a relatively thin crust. It demonstrates that a 1% positive density anomaly of possible mafic/ultramafic cumulates (e.g., pyroxenite, eclogite) from the sub-arc lithosphere is sufficient to induce dynamic downwelling (Fig. 3 and Supplementary Video 1). The dense volcanic root sinks vertically through the mantle, reaching a depth of approximately 400 km in 10 Ma. Its tilt arises naturally due to relative motion between the surface plate (to the right in our model shown in Fig. 3) and underlying mantle; indeed, lateral motion of the plate leads to a horizontal offset of 150 km between the near-surface departure point and the base of the instability at 400 km, which is compatible with the offset inferred from the seismological images and our estimate of regional lithospheric thickness. The progressive development and foundering of the lithospheric mantle results in a clear pattern of subsidence and uplift (Fig. 3); the vertical load of the density seed initially pulls down the crust, generating subsidence above the drip, but as the drip descends into the mantle and its impact at the surface wanes, we observe a systematic and gradual topographic rebound.

One of the most intriguing features of our model predictions is the extensive thinning of the region of thickest crust, promoted by the lithospheric instability as it sinks into the underlying mantle. Analysis of the stress state in our simulations indicates that this region, which is analogous to the Crocker Range, is under an extensional stress regime, as highlighted

by the principal directions of tension (Supplementary Information Fig. 5). The distance between two points in the lower crust, measured via Lagrangian particles (Fig. 4), is strongly time-dependent, with rapid stretching of ~8 mm/yr over the first Myr of the simulation, which progressively decreases to 1.2 mm/yr from 4-5 Myr and, subsequently, close to 0.25 mm/yr. This demonstrates a direct link between extension and the evolution of the downwelling drip, a link that is further highlighted by additional tests discussed in the next Methods section and illustrated in Extended Data Fig. 6. Indeed, 10 Myr after onset of the simulation, the Moho is ~20% shallower in the region of initially thickened crust. As soon as deformation localizes in such a region, the feedback between the flow field and viscosity ensures that areas of weakness are maintained as the simulation evolves (Extended Data Fig. 7 and Supplementary Video 2). Although our simulations do not capture this aspect, it is possible that further crustal extension is facilitated via deep crustal flow associated with loading induced by growth of Mt Kinabalu. As expected, considerable stretching of the crust leads to elevated temperatures at shallower depths (Fig. 3, 4 and Extended Data Fig. 8), which would facilitate melting of the lower crust and emplacement of Mt Kinabalu. Burton-Johnson et al. (2017) suggested an initial temperature for granitoids of a similar composition to those that generated the granitic units of Mt Kinabalu equal to 670-700 ˚C, consistent with the upward deflection of the deeper isotherms shown in Fig. 4. This is corroborated by the comparison of our model temperature to the water-saturated solidus curve applicable to a granitic composition (*30*), which indicates melting conditions are met at ~35 km depth (Extended Data Fig. 8). The density-dependent isostatic rebound of the granitic rocks of Mt Kinabalu could explain their subsequent rapid exhumation and uplift (*31*). In our geodynamical model, the instability does not fully detach from the lithosphere (Fig. 3 and 5); it is important to note that such narrow connections lie beyond the resolution limit (~ station spacing) of our seismic imaging, although a slightly wider region of low temperature surrounds the density anomaly (see Extended Data Fig. 8 and

Supplementary Video 2), which could somewhat contribute to increase the seismic velocities. Composition is also known to affect seismic velocities and our conversion from model P-T to seismic velocity structure (Methods, Extended Data Fig. 8) confirms that our synthetic seismic velocity perturbations are compatible with the shape and magnitude of those observed in our P-wave tomographic model, if we assume the drip has an eclogitic composition, relative to a pyrolytic background ambient mantle. Nonetheless, relatively low P-wave perturbations in the upper mantle beneath Semporna Peninsula (approximately -0.4 km/s dVp) do point towards possible asthenospheric upwelling, as do shallow upwelling velocities predicted in our simulations (Fig. 5 and Supplementary Video 1), and predicted peridotite melt fractions that exceed 1% above the drip (Extended Data Fig. 9). Future work should carefully examine how the dynamics of the drip would be modified in 3-D and by background mantle flow induced by remnant slabs and adjacent subduction systems.

The relatively small and transient nature of lithospheric drips mean that they are rarely imaged seismically; as such, their important role in the evolution of arc-complexes and subduction zones, following subduction termination, may have been overlooked. While a link between lithospheric drips and intraplate magmatism, topographic changes and extension have been suggested (e.g., *17,18,21,23*), our study delivers interdisciplinary insights into post-subduction dynamics and processes, providing a conceptual template for predicting the widespread effects of lithospheric foundering following subduction termination. Our simulations imply that post-subduction lithospheric drips, even if relatively small, may be an important transitional process in the evolution of any arc-trench complex, causing extensive deformation even in areas far from the location of initial downwelling. The mechanism we propose here may play a major role in shaping regional tectonics, requiring reinterpretation of areas recently affected by subduction termination, including the Carpathians-Pannonian region, western United States, the Betic-Rif orogen and the eastern Mediterranean region.

Acknowledgments S.P. acknowledges support from the Natural Environmental Research Council (NERC) Grant NE/R013500/1 and from the European Union's Horizon 2020 Research and Innovation Program under Marie Skłodowska-Curie Grant Agreement 790203. We thank the TanDEM-X Science Communication Team (German Aerospace Center (DLR) e.V.) for providing TanDEM topographic data. We thank the NERC Geophysical Equipment Facility for loan 1038. Numerical simulations were undertaken on the NCI National Facility in Canberra, Australia, which is supported by the Australian Commonwealth Government. A.G. was funded by an Independent Research Fellowship from the Royal Astronomical Society.

Contributions

S.P. conceived this study, created the P-wave tomographic model, integrated all observational constraints, and made all figures. S.P. performed the numerical simulation with guidance from D.R.D., building on developments by D.R.D., S.C.K. and C.R.W.

S.P., D.R.D. and R.H. made the main interpretation. C.B. measured azimuthal anisotropy. A.G. created the crustal thickness map. T.G. created the lithospheric thickness map. S.G. converted the P-T model to seismic velocity. S.P., C.B., A.G., T.G., F.T., D.C. and N.R. participated in the seismic field acquisition. N.R., S.P. and A.G. acquired funding for this study. N.R. and F.T. conceived the nBOSS experiment.

S.P. wrote the paper, following discussion with, and contributions from, all authors.

Competing interests

The authors declare no competing financial interests

Figures

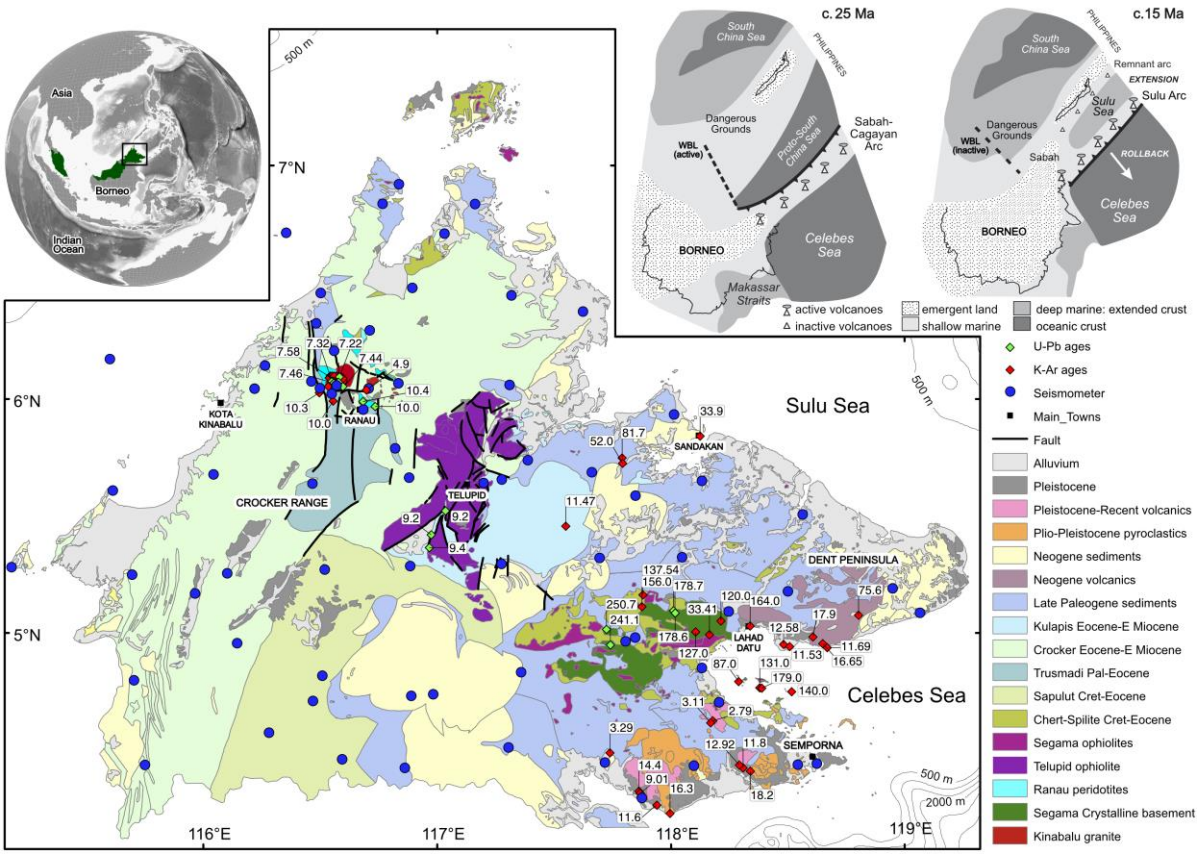

Fig. 1: Geological map of Sabah with seismic stations of nBOSS and MetMalaysia. Surface geology information and geochemical dating from the study area (*1*). Inset in the upper left corner shows Malaysia in dark green and Sabah within the black rectangle. Inset in the upper right corner summarizes the tectonic evolution of Borneo and the Sulu Sea in the late Paleogene and mid-Miocene (modified from Hall, 2013). WBL – West Baram Line.

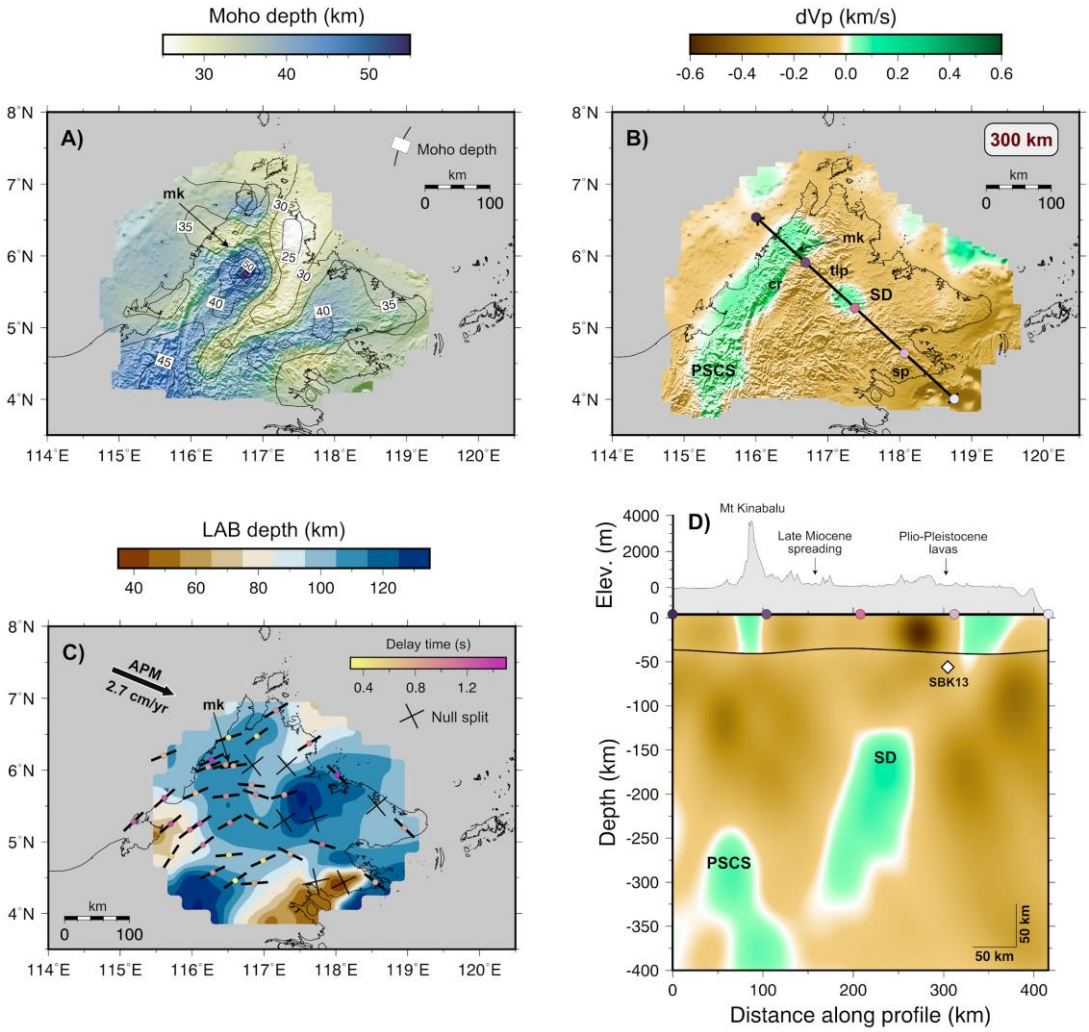

Fig. 2: Crustal thickness, lithospheric thickness, anisotropy and P-wave tomographic model. A) Depth-to-Moho estimates determined by receiver-function analysis. B) Horizontal slice at 300 km depth taken from the final tomographic solution model. Black line and colored dots indicate the location of the vertical profile presented in D). C) Fast-polarization orientations from core-refracted shear phases superimposed onto a lithospheric thickness map. Arrow indicates the absolute plate motion direction (ITRF reference frame - *24*). White diamond in D) denotes the approximate location of sample SBK13. SD: Semporna Drip; PSCS: Proto-South China Sea; mk: Mt Kinabalu; cr: Crocker Range; sp: Semporna Peninsula; tlp: Telupid.

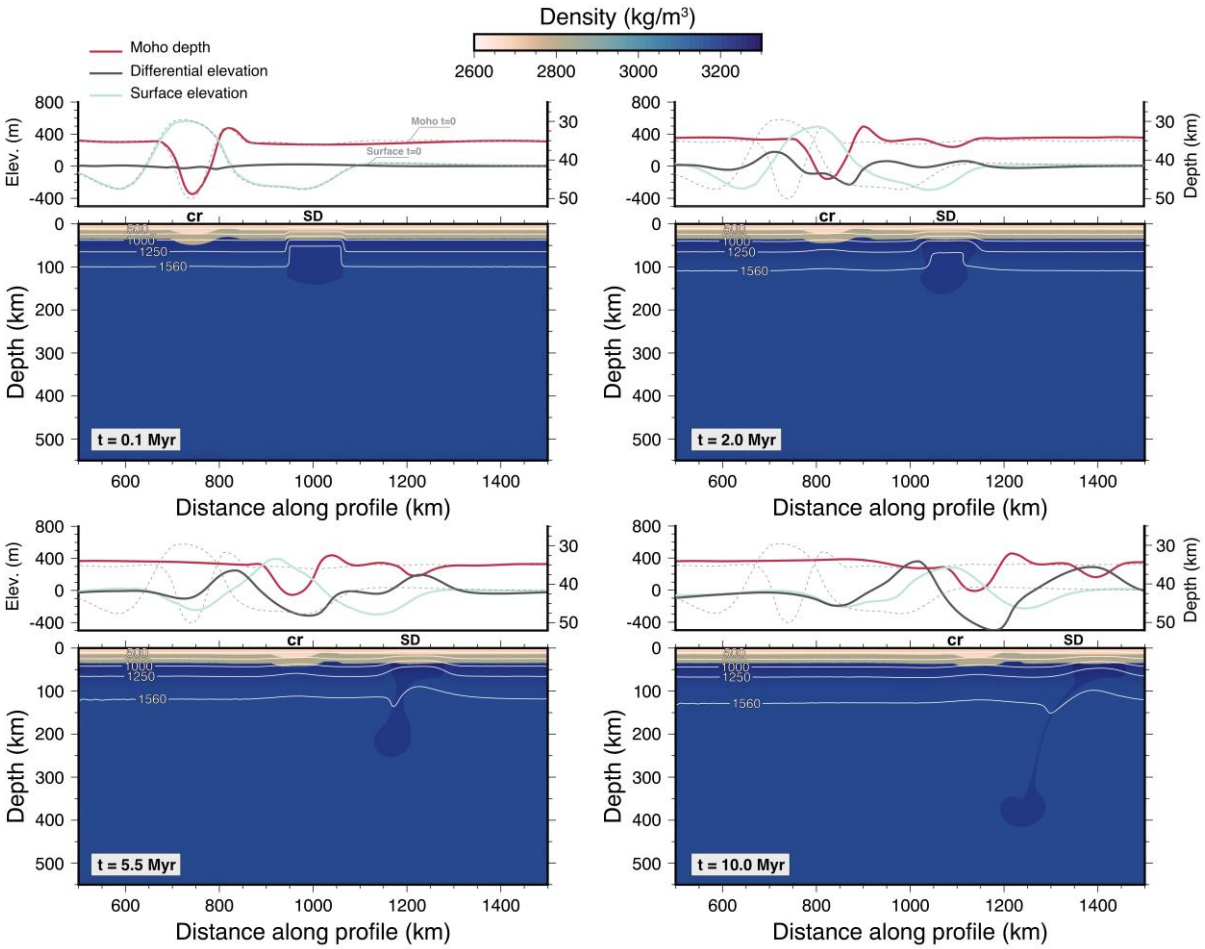

Fig. 3: Temporal snapshots illustrating the evolution of a lithospheric drip from our simulation: time (t) in Myr from the start of the simulation. White lines are isotherms in Kelvin. A thick, higher density seed is centered at x=1000 km, approximating mafic cumulates beneath a volcanic arc. Moho (interface between crustal and mantle material volume fraction fields) and surface elevation evolution are illustrated above each panel. The differential elevation is calculated by subtracting the surface elevation at time 0 from that at a specific timestep, accounting for the prescribed plate motion at 4 cm/yr. Note how the area of thick crust (cr) undergoes significant thinning and the Moho becomes shallower. Similarly, subsidence accompanies initial sinking of the drip, which is then followed by vertical rebound as the lower lithosphere is removed. cr: Crocker Range; SD: Semporna drip.

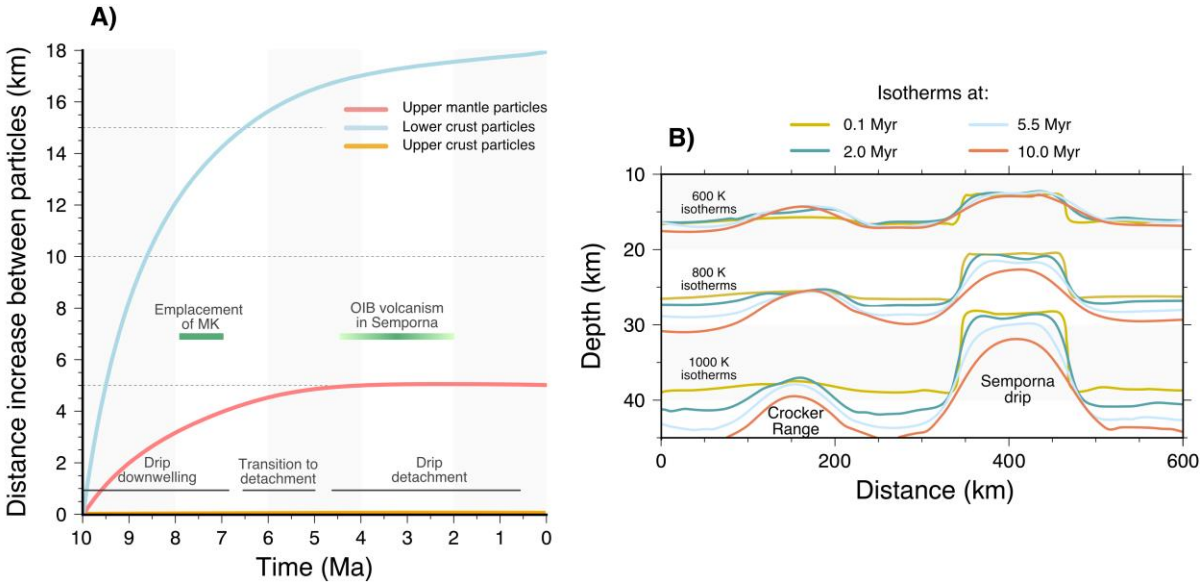

Fig. 4: Stretching in the Crocker Range and upward deflection of isotherms. A) The increase in distance between two particles located in the upper crust (orange), lower crust (light blue) and upper mantle (light red) throughout the simulation. Zero distance corresponds to simulation onset, where all particles are 100 km apart. Time is expressed in Ma (million years before present) to match the age of the main tectonic events (10 Ma equals onset of simulation). Particle locations are also shown in Supplementary Information Fig. 5 with consistent colors. Increasing distance between particles is a proxy for extension in the Crocker Range, which is intimately tied to the drip, as it descends away from the surface into the underlying mantle. B) Evolution of 600, 800 and 1000 K isotherms at different stages of the simulation. Extension in the lower crust of the Crocker Range is accompanied by an upward deflection of these isotherms relative to adjacent areas. To allow for straightforward comparison, isotherms from different simulation times have been aligned under the area of thick crust, coincident with the Crocker Range.

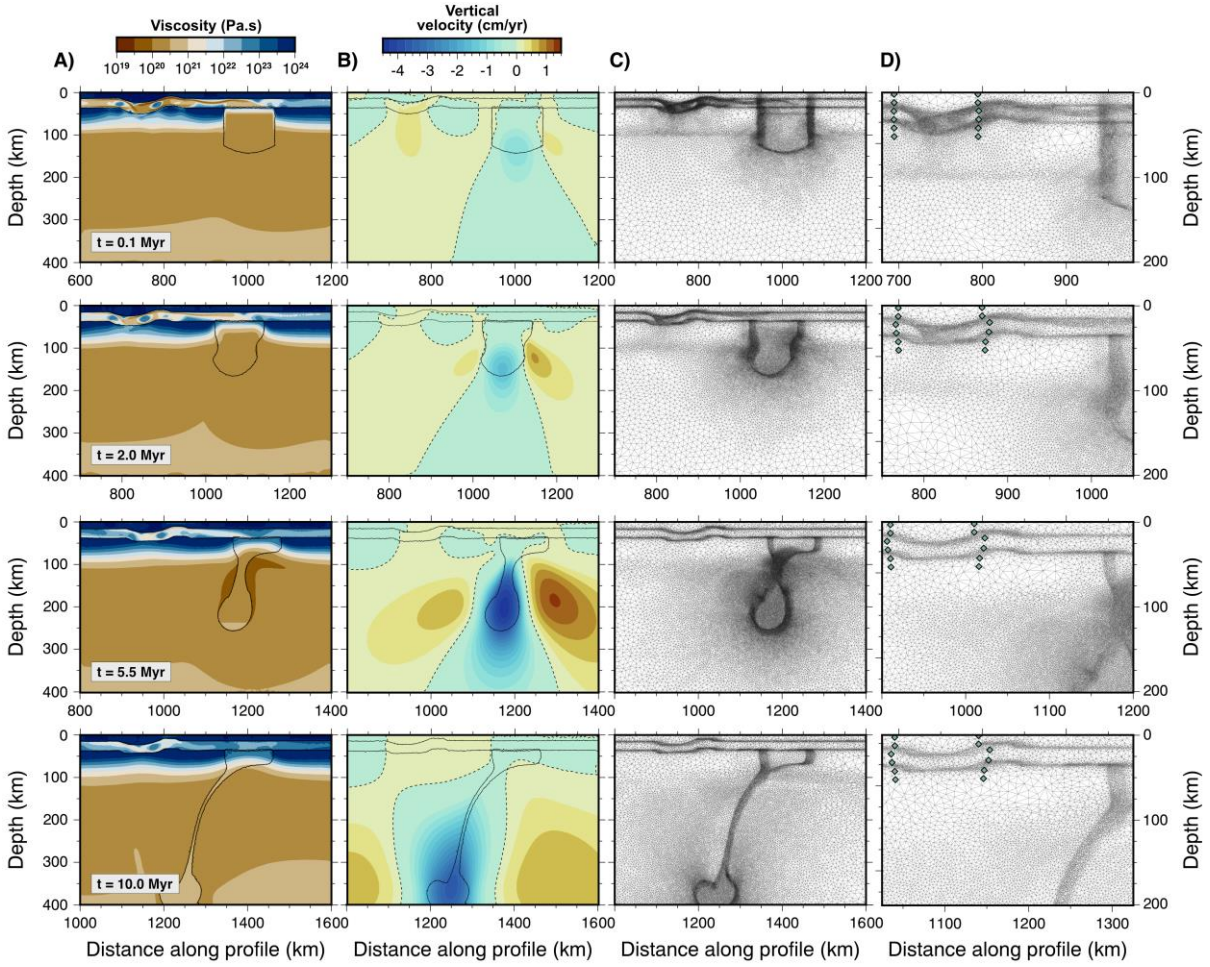

Fig. 5. Viscosity, vertical velocity and adaptive mesh. A) viscosity at different stages of the model; B) vertical velocity with negative and positive values indicating downwelling and upwelling, respectively. Dashed black line delineates the zero vertical velocity contour. Note that within a few Myr of drip initiation, vertical velocities become positive beneath the Crocker Range, an essential process that would facilitate melting; C) the associated computational mesh; D) a zoom-in of C), also illustrating particle locations. Our adaptive mesh approach achieves minimum edge-lengths of 600 meters in regions of dynamic significance (i.e., at material interfaces and in areas of high temperature and velocity gradient), with coarser resolution of up to 50 km, elsewhere. This high-resolution is essential for accurately and efficiently capturing key elements of our simulation.

Main References

1. Lai, C.K., Xia, X.P., Hall, R., Meffre, S., Tsikouras, B., Rosana Balangue-Tarriela, M.I., Idrus, A., Ifandi, E. and Norazme, N.A. Cenozoic Evolution of the Sulu Sea Arc-Basin System: An Overview. *Tectonics,* **40**, (2021).
2. Hall, R. Reconstructing Cenozoic SE Asia. *Geol. Soc. Spec. Publ.* **106,** 153-184 (1996).
3. Cullen, A. B. Transverse segmentation of the Baram-Balabac Basin, NW Borneo: Refining the model of Borneo's tectonic evolution. *Petroleum Geoscience,* **16,** 3–29 (2010).
4. Wu, J., & Suppe, J. Proto-South China Sea plate tectonics using subducted slab constraints from tomography. *J. Earth Sci.,* **29,** 1304–1318 (2018).
5. Hall, R. Contraction and extension in northern Borneo driven by subduction rollback. *J. Asian Earth Sci.,* **76,** 399-411 (2013).
6. Hutchison, C.S., Bergman, S.C., Swauger, D.A. & Graves, J.E. A Miocene collisional belt in north Borneo: uplift mechanism and isostatic adjustment quantified by thermochronology. *J. Geol. Soc.*, **157,** 783-793 (2000).
7. Bergman, S., Hutchison, C., Swauger, D., & Graves, J. K-Ar ages and geochemistry of the Sabah Cenozoic volcanic rocks. *Bull. Geol. Soc. Malays.*, **44,** 165– 171 (2000).
8. Tsikouras, B., Lai, C. K., Ifandi, E., Teo, C. H., & Xia, X. P. New zircon radiometric U-Pb ages and Lu-Hf isotopic data from the ultramafic-mafic sequences of Ranau and Telupid (Sabah, eastern Malaysia): Time to reconsider the geological evolution of Southeast Asia?. *Geology,* (2021).
9. Cottam, M., Hall, R., Sperber, C. & Armstrong, R. Pulsed emplacement of the Mount Kinabalu granite, northern Borneo. *J. Geol. Soc.*, **167,** 49-60 (2010).

10. Cottam, M.A., Hall, R., Sperber, C., Kohn, B.P., Forster, M.A. and Batt, G.E. Neogene rock uplift and erosion in northern Borneo: evidence from the Kinabalu granite, Mount Kinabalu. *J. Geol. Soc.*, **170,** 805-816 (2013).

11. Morley, C.K. & Back, S. Estimating hinterland exhumation from late orogenic basin volume, NW Borneo. *J. Geol. Soc.*, **165,** 353-366 (2008).

12. Balaguru, A. & Nichols, G. Tertiary stratigraphy and basin evolution, southern Sabah (Malaysian Borneo). *J. Asian Earth Sci.*, **23,** 537-554 (2004).

13. Macpherson, C.G., Chiang, K.K., Hall, R., Nowell, G.M., Castillo, P.R. and Thirlwall, M.F. Plio-Pleistocene intra-plate magmatism from the southern Sulu Arc, Semporna peninsula, Sabah, Borneo: Implications for high-Nb basalt in subduction zones. *J. Volcanol. Geotherm. Res.*, **190,** 25-38 (2010).

14. Simons, W.J.F., Socquet, A., Vigny, C., Ambrosius, B.A.C., Haji Abu, S., Promthong, C., Subarya, C., Sarsito, D.A., Matheussen, S., Morgan, P. and Spakman, W. A decade of GPS in Southeast Asia: Resolving Sundaland motion and boundaries. *J. Geophys. Res.*, **112,** (2007).

15. Houseman, G.A., McKenzie, D.P. and Molnar, P. Convective instability of a thickened boundary layer and its relevance for the thermal evolution of continental convergent belts. *J. Geophys. Res.*, **86,** 6115-6132 (1981).

16. Zandt, G., Gilbert, H., Owens, T.J., Ducea, M., Saleeby, J. and Jones, C.H. Active foundering of a continental arc root beneath the southern Sierra Nevada in California. *Nature,* **431,** 41-46 (2004).

17. Levander, A., Schmandt, B., Miller, M.S., Liu, K., Karlstrom, K.E., Crow, R.S., Lee, C.T. and Humphreys, E.D. Continuing Colorado Plateau uplift by delamination-style convective lithospheric downwelling. *Nature,* **472,** 461-465 (2011).

18. Göğüş, O.H., Pysklywec, R.N., Şengör, A.M.C. and Gün, E. Drip tectonics and the enigmatic uplift of the Central Anatolian Plateau. *Nat. Comm.,* **8,** 1-9 (2017).

19. West, J.D., Fouch, M.J., Roth, J.B. and Elkins-Tanton, L.T. Vertical mantle flow associated with a lithospheric drip beneath the Great Basin. *Nat. Geosci.,* **2,** 439-444 (2009).

20. Molnar, P. Gravitational instability of mantle lithosphere and core complexes. *Tectonics*, **34**, 478-487 (2015).

21. Houseman, G.A. and Gemmer, L. Intra-orogenic extension driven by gravitational instability: Carpathian-Pannonian orogeny. *Geology*, **35,** 1135-1138 (2007).

22. Elkins-Tanton, L.T. Continental magmatism, volatile recycling, and a heterogeneous mantle caused by lithospheric gravitational instabilities. *J. Geophys. Res. Solid Earth,* **112,** B03405, (2007).

23. Wang, H. and Currie, C.A. Magmatic expressions of continental lithosphere removal. *J. Geophys. Res. Solid Earth,* **120,** 7239-7260 (2015).

24. Altamimi, Z., Rebischung, P., Métivier, L. and Collilieux, X. ITRF2014: A new release of the International Terrestrial Reference Frame modeling nonlinear station motions. *J. Geophys. Res. Solid Earth,* **121**, pp.6109-6131 (2016).

25. Roberts, G.G., White, N., Hoggard, M.J., Ball, P.W. and Meenan, C. A Neogene history of mantle convective support beneath Borneo. *Earth Planet. Sci. Lett.*, **496,** 42-158 (2018).

26. Hall, R. & Spakman, W. Mantle structure and tectonic history of SE Asia. *Tectonophysics,* **658,** 14-45 (2015).

27. Duretz, T., Gerya, T.V. and May, D.A. Numerical modelling of spontaneous slab breakoff and subsequent topographic response. *Tectonophysics*, **502**, 244-256 (2011).

28. Jones, C.H., Reeg, H., Zandt, G., Gilbert, H., Owens, T.J. and Stachnik, J. P-wave tomography of potential convective downwellings and their source regions, Sierra Nevada, California. *Geosphere*, **10**, 505-533 (2014).

29. Burton-Johnson, A., Macpherson, C.G. and Hall, R. Internal structure and emplacement mechanism of composite plutons: evidence from Mt Kinabalu, Borneo. *J. Geol. Soc.*, **174**, 180-191 (2017).

30. Wyllie, P.J. Crustal anatexis: an experimental review. *Tectonophysics*, **43,** 41-71 (1977).

31. Braun, J., Simon-Labric, T., Murray, K.E. and Reiners, P.W. Topographic relief driven by variations in surface rock density. *Nat Geosc*, **7**, 534-540 (2014).

METHODS

Crustal thickness estimates

Three-component seismograms for earthquakes of magnitude larger than 5, occurring between 30˚ and 90˚ epicentral distance from Sabah, were extracted from the continuous data records of the nBOSS and MetMalaysia seismic networks (Extended Data Fig. 1). A total of 85,518 seismograms were inspected and only those where the P arrival signal-to-noise ratio was high were taken forward for further analysis. After this initial quality control, a total of 14,447 seismograms were used to calculate radial receiver functions using the time-domain iterative deconvolution method (*32*) with a maximum frequency of approximately 1 Hz.

Receiver functions with a fit of less than 70% between the receiver function estimate convolved with the observed vertical component and the observed radial component were discarded. The remaining receiver functions were visually inspected and discarded if they appeared noisy, oscillatory, or anomalous compared to other receiver functions from a similar distance and backazimuth. This final quality control left a remaining dataset of 3,862 receiver functions. All the receiver functions at an individual station (Supplementary Information Fig. 1 shows those for stations SBA8) were stacked together to reduce noise, yielding a stacked receiver function that is subsequently used in the joint inversion for shear-velocity structure.

1-D fundamental mode Rayleigh-wave group-velocity dispersion curves were extracted from the GDM52 global compilation (*33*) for each station location for a period range 25–250 s. Since the period range 25–250 s only constrains velocities in the lower crust and below, the surface wave data are primarily used here to ensure that the shear velocity values are realistic for this region to overcome the Vp/Vs-depth trade-off inherent in receiver-function data.

Dispersion curves and radial P receiver-function stacks for each station were inverted for shear-velocity structure using *joint96* (*34*), an iterative non-linear least squares inversion method. Inversions are allowed to run until the misfit reduction is 0.005% of its initial value, hence the number of iterations in the inversion is not the same for each station. Several different starting models have been tested including constant values of 4.48 km/s, which is the uppermost mantle velocity in the ak135 model (*35*), 4.28 km/s, and 3.70 km/s, and a Vp/Vs value of 1.79 down to 100 km, parameterized into 2 km thick layers, overlying ak135. Because none of these models preconditions crustal thickness, Moho structure recovered by the inversion is largely a function of the data. While there are some small variations between the solutions produced by the different starting models, they are sufficiently similar to not alter the interpretation of the structure.

In *joint96*, the relative weights for the receiver function and surface wave data are given by the p value, where the smaller the number, the greater the contribution from receiver functions. A p value of 0 means the inversion only includes receiver function data; a p value of 1 only includes surface wave data. We seek the model that has the maximum contribution from receiver functions but that maintains a good fit to the surface wave data, because the receiver functions have the greatest sensitivity to discontinuities such as the Moho. We tested p values of 0.5, 0.1, 0.05, and 0.01 (Supplementary Information Fig. 1). Overall, the models show little variation in structure with p value, indicating that the resulting structures are robust.

The depth of the Moho beneath each station is picked from the 1-D shear velocity model, at the depth that corresponds to the base of the steepest positive velocity gradient where shear velocity exceeds 4 km/s.

Shear-wave splitting analysis

When a linearly polarized shear wave impinges on an anisotropic medium, it is partitioned into two quasi-S waves, which propagate with different wave-speeds. The polarization of these two waves, commonly called 'fast' (Π) and 'slow', is determined by the symmetry and orientation of the anisotropic elastic tensor. A time lag (dt) accrues between the waves while they propagate through the region, with the final integrated value proportional to both the path length and strength of anisotropy.

A catalogue of viable earthquakes was produced containing only events with Mb $\geq$ 5.8 and epicentral distance $\geq$85˚, resulting in a total of 129 events. Arrival times for (S,SK,P,PK,SKI,PKI)KS phases were predicted from a traveltime lookup table for each event/station pair. All waveform data were bandpass filtered between 3 and 25 s before a signal-to-noise ratio was calculated in a window around the theoretical arrival time. Only XKS arrivals with a signal-to-noise ratio exceeding 1.5 were retained for splitting analysis. The waveform data were then inspected and the automatically assigned analysis windows were re-picked, where necessary, to best capture the phase arrival. Poor quality, noisy waveforms were also removed at this stage. The initial splitting analysis was performed using a single channel transverse energy minimization method (*36*), as implemented in the SplitRacer toolkit (*37*), assuming a horizontal layer of anisotropic medium. The resulting splitting measurements were then visually inspected and classified as 'good' (clear and well-constrained splitting), 'fair' (clear evidence of splitting, but less well-constrained), 'null' (clear absence of splitting), and 'poor' (indeterminable result). Measurements classified as 'poor' were disregarded in further analysis. Final station estimates are determined by averaging 'good' and 'null' observations through the single-layer error surface stacking method of Wolfe and Silver (*38*).

We present shear-wave splitting measurements at 62 stations across Sabah. 46 of these measurements stem from the nBOSS network, while the remaining 16 are from MetMalaysia

instruments. Of these 16, one site (KKM, near Mt Kinabalu) has been in continuous operation since 2006, with data archived on the IRIS data center. At this site there is little evidence of splitting parameters varying as a function of back-azimuth, though this does not preclude the possibility of second-order effects at other stations. The lack of shear-wave splitting measurements prevents us from investigating this further. Supplementary Information Fig. 2 shows a good splitting measurement from station SBA8. Most of the null measurements at stations in central and western Sabah appear to be geometric (i.e., the back-azimuth is approximately aligned with the expected fabric). While anisotropy is likely to be present below these stations, we do not have good events at the right back-azimuths to validate this. Nulls detected in the Semporna Peninsula are not well aligned with one of the nominal fast/slow axes, and hence are considered to be true nulls.

Lithospheric thickness estimate

The shear-wave velocity (Vs) model is calculated by initially inverting for phase velocities at periods between 25 and 200 s using a total of 225 teleseismic sources. We implement a two-plane-wave approach (*39*) and analytical sensitivity kernels (*40*). Pseudo-dispersion curves are extracted on a 0.2° grid at locations where the formal error from the least-squares inversion is less than 0.6 km/s. These are inverted for Vs using a reversible jump, Markov-chain Monte-Carlo method (*41*). Based on synthetic recovery tests, we estimate that regions with more than 10 dispersion observations contain robust solutions. We convert our Vs model to temperature using the equation (*24,41*) $V_s = \big(1 + b_v(z - 50)\big)\big(m(T - 273) + c + Aexp(-E - PV_a)/RT\big)$, where z is the depth (in km), T is the temperature (in K) and b_v, c, A, E, m and V_a are empirically fitted constants with the values of 3.84 × 10-4 km^{-1}, 4.72 km s^{-1}, -1.8 × 1016 m s^{-1}, 409 KJ mol^{-1}, -2.8 × 10-1 m s^{-1} and 10 × 10-6 m^3 mol^{-1}, respectively. The pressure is assumed to be lithostatic and is calculated as $P = \rho g z$, where ρ is the density (3330 kg m^{-3}) and g is the

acceleration due to gravity (9.81 ms^{-2}). The LAB is assumed to be a constant temperature of 1333°C (*42*). Thus, we assume the depth to the LAB is the depth to the 1333°C contour, which is consistent with the estimated temperature in the mantle beneath Sabah from sample SBK13 (*25*). Lowering the mantle potential temperature would drastically increase the region of lithospheric removal, which would be inconsistent with the record of magmatism in the region.

P-wave traveltime inversion

A total of 787 teleseismic sources were initially selected from the ISC catalogue; this includes all earthquakes from any depth with Mb larger than 5, and Mb larger than 4.6 if it occurred at a depth greater than 150 km.

A variety of P-wave phases, including direct P, pP, Pdiff, ScP, PcP and PKiKP are targeted and extracted from the continuous seismic dataset after the application of a bandpass filter with corner frequencies of 0.05 and 4 Hz. While most of the arrival times are typically from first-arriving P waves, the addition of core and reflected phases means that we can use seismic rays from outside the typical epicentral distance of 27˚-90˚, which can have different incidence angles. All extracted seismic traces have been initially aligned using the ak135 model (*35*) (Supplementary Information Fig. 3) and stacked to produce an initial reference trace. Relative P-wave traveltime residuals have been subsequently extracted using an adaptive stacking technique (*43)*, which uses the coherency of global phases across the entire network. Iterative improvement of the alignment by comparing the reference trace with each station trace is applied, which ultimately leads to an estimate of the residuals and associated picking error.

At this stage, all sources recorded by at least seven stations, with an average uncertainty estimate of the residuals below 0.12 seconds, are retained (see Supplementary Information Fig. 4 for two examples of arrival-time residual maps). After visually inspecting and selecting

traveltimes on a source-by-source basis, 30671 residual times are used to invert for 3-D velocity structure. This is achieved by using a grid-based eikonal solver and a subspace inversion technique implemented in FMTOMO (*44*). Crustal thickness variations inferred from receiver function are directly included in FMTOMO during the inversion. Similarly, shear-wave velocities derived from receiver function analysis are converted into P-wave velocities according to the formulation of Brocher (*45*) and included in the inversion to correct for crustal-velocity variations. While the Moho is kept fixed during the inversion, crustal velocities are inverted for.

The non-linearity of the inverse problem is addressed by running six iterations of the subspace scheme, and updating the ray path and traveltime information using the multistage Fast Marching Method at the end of each iteration. The level of imposed regularization is controlled by the damping and smoothing parameters, calibrated after examination of L-curves to provide the optimum tradeoff between data fit and model roughness. Our final tomographic model, shown through a series of horizontal slices in Extended Data Fig. 2, yields a variance reduction of 87%.

In order to confirm the dip and spatial extent of the high-velocity anomaly presented in Fig. 2D (SD) of the main text, we have conducted a number of resolution tests based on synthetic data. The synthetic data are created by applying the forward calculator (FMM), using the same source-receiver configuration as the observational dataset, in the presence of synthetic structure resembling a vertical and a tilted drip, and adding Gaussian noise with a standard deviation of 100 ms in order to simulate the noise content of real data, which includes picking uncertainty. As in the inversion of observed residual arrival-times, the 3-D volume is discretized into two layers (crust and mantle) with the spatial distribution of velocity nodes equal to 20 km in all directions, and every 10 km for the propagation grid (used by FMM in

the forward step). Examples of the resolution tests are shown in Extended Data Figs. 3 and 4, which indicate that both the vertical and lateral location of the synthetic high-velocity anomaly is resolved with a high degree of confidence. Additionally, our synthetic tests demonstrate that we can recover with equal confidence the dip of the synthetic structure, while the level of vertical smearing is relatively minor (as suggested by the spike test in Extended Data Fig. 4).

Thermo-mechanical simulation(s)

We simulate the dynamics, evolution and tectonic and geological consequences of a lithospheric drip using Fluidity, a finite element, control-volume, adaptive mesh computational modeling framework (*46,47*). Fluidity has been extensively tested, verified and validated for geodynamical simulations of this nature. The numerical approach uses anisotropic, dynamically adaptive mesh optimization (Fig. 5 and Supplementary Video 2), to provide high-resolution in areas of dynamic importance. We focus on idealised models of a lithospheric instability, in order to isolate its influence on the diagnostics that we examine (e.g., topography, stress, stretching). Future work should analyse how our conclusions are modified in the presence of additional complexities. However, focussing on idealised models has allowed us to isolate the significance of a drip in driving a complex response at Earth's surface.

Our initial model setup is illustrated in Extended Data Fig. 5, with key model parameters listed in Extended Data Table 1. The model is executed in a 2-D domain of dimensions 2000 x 660 km. We solve the incompressible Stokes, continuity and energy equations, under the Boussinesq approximation. We also track volume fractions representing four different materials (upper crust, lower crust, seed and mantle), using a control-volume discretization with a minimally diffusive HyperC face-value scheme, that ensures conservation and boundedness by coupling the fluxes between the volume fractions (*48)*. Mechanical boundary conditions include a free-surface top, incorporating mesh movement with a prescribed 4 cm/yr

horizontal velocity, a zero-slip base, and open hydrostatic sides. We decided to adopt in our simulation a plate velocity of 4 cm/yr, since it produces a final dip of the lithospheric drip that more closely resembles that observed seismically. Thermal boundary conditions are prescribed to 273 K at the surface and 1573 K at the base of the model. The inflow boundary is prescribed at a temperature that matches its initial condition, with a free outflow boundary. The Moho temperature is set to 973 K (*49*). We include internal heating, at different rates for upper crust, lower crust and underlying mantle. Initial thermal conditions are different above a density seed that is 120 km (approximate width of Sulu arc) in width and 140 km in height from the surface, centered at x=1000 km, where the Moho temperature is higher (1173 K), consistent with petrological and seismic constraints from modern arcs (*50*), and the thermal LAB is at 50 km depth. While the vertical extent of the density seed is somewhat larger than used in some studies, its width is narrower (*18,21,23*), but is consistent with the width that we have inferred from seismic images. Our initial conditions include a region of thick crust (inferred from Fig. 2A), approximating the Crocker Range, believed to have formed by continental collision between the Dangerous Grounds and western Sabah (*2-5,6*). Adjacent to a region of thick crust we have a thinner crust (30 km thickness), believed to have been extended through rollback associated with trench retreat (*5,8*). Our initial conditions for the free-surface height are calculated *a priori* to balance forces induced by underlying crustal-thickness variations.

We implement a composite viscosity (dependent on temperature, pressure and second invariant of strain-rate) based on four deformation mechanisms (*51*) (diffusion creep, dislocation creep, Peierls creep and yielding – as shown in Extended Data Fig. 7). Following *(51)*, diffusion, dislocation, and Peierls creep viscosities are calculated via a generic relationship between stress and strain-rate for each mechanism:

$$\mu_{diff,disl,P} = A^{-\frac{1}{n}} \exp\left(\frac{E + PV}{nRT_r}\right) \dot{\varepsilon}_{II}^{\frac{1-n}{n}}$$

where A is a prefactor, n the stress exponent, E the activation energy, V the activation volume, P the lithostatic pressure, R the gas constant and $\dot{\varepsilon}_{II}$ the second invariant of the strain-rate tensor. Tr is the temperature obtained by adding to the Bousinessq solution an adiabatic gradient of 0.5 K/km.

Yielding is implemented through a brittle-failure type yield-stress law,

$$\mu_y = \frac{\tau_y}{2\dot{\varepsilon}_{II}}$$

with μy the yielding viscosity and τy the yield strength, given by:

$$\tau_y = \min(\tau_0 + f_c P, \tau_{y,max})$$

with τ_0 the surface yield strength, f_c the friction coefficient and $\tau_{y,max}$ the maximum yield strength. The effective viscosity is calculated via a harmonic mean (*50*), with viscosity subsequently capped at lower and upper limits (see Extended Data Table 1):

$$\mu = \left(\frac{1}{\mu_{diff}} + \frac{1}{\mu_{disl}} + \frac{1}{\mu_y} + \frac{1}{\mu_P}\right)^{-1}$$

Calculations for melt fractions are based on a parameterisation for peridotite mantle melting (*52*), recently updated (*53*). We assume a water content of 1000 ppm, which is plausible for an area recently hydrated by subduction.

We have undertaken a systematic series of tests to isolate the key factors controlling the dynamics of our simulations, with results presented in Extended Data Fig. 6. In the first of these tests (T1_Strong), a flat, stronger crustal layer is sufficient to prevent lower-crustal extension in response to motion of the drip. This demonstrates that a weak lower crust (e.g., *54*, *55*) is a fundamental requirement for drip-induced extension. We note that a weak lower

crust is plausible in this region, since subduction (e.g., through hydration of the upper plate) and continent-continent collision (e.g., through thickening and consequent heating) can induce significant rheological weakening. The second series of tests demonstrate that localization of extension beneath the Crocker Range requires asymmetric strength on either side of the drip (T2_Asym). In our main simulation, this is facilitated by crustal thickness variations to the west of the drip - if such heterogeneity is not present, extension will be symmetric on both sides of the drip (T2_Sym). The third series of tests (T3_PM) confirm that plate motion is a fundamental requirement to reproduce the observed tilt of the drip, although it only weakly modulates lower crustal extension. Finally, our last test (T4_Buoy) demonstrates that only a small fraction of crustal uplift and lower-crustal extension is driven by the positive buoyancy of the thickened crust. Taken together, these results strongly support a direct link between the Semporna drip, the evolution of regional topography, and lower-crustal extension beneath the Crocker Range.

P-T conversion to dVp

Mantle mineralogy models (*56*,*57*) allow mapping of seismic heterogeneity to thermal and density variations for a given mantle composition. The dependence on pressure translates directly to depth (*58*). For Vp variations, the temperature dependence is mostly affected by elastic (anharmonic) effects. We obtain a look-up table for mantle minerals by assuming: (i) a pyrolitic mantle, consistent with the bulk of mantle minerals, and (ii) eclogitic material representing the lithospheric drip. The relevant stable mineral phases are computed using the solution parameters compiled by (*57*) in the *PerpleX* software (*59*).

Data availability

Part of the nBOSS dataset is accessible through the IRIS Data Management (see https://www.fdsn.org/networks/detail/YC_2018/). Data from the remaining nBOSS stations will be available from February 2024. Data from the Malaysian national seismic network (https://www.fdsn.org/networks/detail/MY/) are restricted but may be obtained by contacting the Malaysian Meteorological Department.

Code availability

The Fluidity computational modelling framework, including source code and documentation, is available from https://fluidityproject.github.io/; the latest release, which was used for the simulations presented herein, has been archived at Zenodo https://doi.org/10.5281/zenodo.5221157. The source code and manual for FMTOMO are available http://iearth.edu.au/codes/FMTOMO/.

Methods References

32. Ligorría, J. P., & Ammon, C. J. Iterative deconvolution and receiver-function estimation: *BSSA* **89**, 1395-1400 (1999).
33. Ekström, G. A global model of Love and Rayleigh surface wave dispersion and anisotropy, 25-250 s: *Geophys. J. Int.* **187**, 1668-1686 (2011)
34. Herrmann, R. B. Computer programs in seismology: An evolving tool for instruction and research. *Seismol. Res. Lett.* **84**, 1081-1088 (2013).
35. Kennett, B. L. N., Engdahl, E. R., and Buland, R. Constraints on seismic velocities in the Earth from traveltimes. *Geophys. J. Int.* **122**, 108-124 (1995).
36. Silver, P. G., & Chan, W. W. Implications for continental structure and evolution from seismic anisotropy. *Nature.* (1988).

37. Reiss, M. C., & Rümpker, G. SplitRacer: MATLAB code and GUI for semiautomated analysis and interpretation of teleseismic shear-wave splitting. *Seismol. Res. Lett.,* **88,** 392-409 (2017).

38. Wolfe, C. J., & Silver, P. G. Seismic anisotropy of oceanic upper mantle: Shear wave splitting methodologies and observations. *J. Geophys. Res. Solid Earth*, **103,** 749-771 (1998).

39. Forsyth, D.W., Li, A., Levander, A. and Nolet, G. Array analysis of two-dimensional variations in surface wave phase velocity and azimuthal anisotropy in the presence of multipathing interference. *Geophys. Monogr.,* **157,** 81 (2005).

40. Yang, Y. and Forsyth, D.W. Regional tomographic inversion of the amplitude and phase of Rayleigh waves with 2-D sensitivity kernels. *Geophys. J. Int.,* **166,** 1148-1160 (2006).

41. Dreiling, J. & Tilmann, F. BayHunter - McMC transdimensional Bayesian inversion of receiver functions and surface wave dispersion. 5 Files (GFZ Data Services, 2019).

42. Priestley, K. & McKenzie, D. The thermal structure of the lithosphere from shear wave velocities. *Earth Planet. Sci. Lett.*, **244,** 285–301 (2006).

43. Rawlinson, N., Kennett, B. L. N. Rapid estimation of relative and absolute delay times across a network by adaptive stacking. *Geophys. J. Int.,* **157,** 332-340 (2004).

44. Rawlinson, N., de Kool, M., Sambridge, M. Seismic wavefront tracking in 3-D heterogeneous media: applications with multiple data classes. *Explor. Geophys.*, **37,** 322-330 (2006).

45. Brocher, T.M. Empirical relations between elastic wavespeeds and density in the Earth's crust. *Bull. Seismol. Soc. Am,* **95,** 2081-2092 (2005).

46. Davies, D. R., Wilson, C. R. and Kramer S. C. Fluidity: A fully unstructured anisotropic adaptive mesh computational modeling framework for geodynamics. *Geochem. Geophys. Geosyst.,* **12,** Q06001 (2011).

47. Kramer, S. C., Wilson, C. R. and Davies, D. R. An implicit free surface algorithm for geodynamical simulations. *Phys. Earth Planet. Inter.*, **194,** 25–37 (2012).

48. Wilson, C. R. Modelling multiple-material flows on adaptive unstructured meshes, PhD thesis, Imp. Coll. London, London (2009).

49. Currie, C. A., Hyndman R. The thermal structure of subduction zone back arcs. *J. Geophys. Res. Solid Earth*, **111,** B08404 (2006).

50. Kelemen, P.B., Rilling, J.L., Parmentier, E.M., Mehl, L., and Hacker, B.R. Thermal structure due to solid-state flow in the mantle wedge beneath arcs, in Eiler, J., ed., Inside the Subduction Factory: *American Geophysical Union Geophysical Monograph* **138**, 293–311 (2003).

51. Garel, F. et al. Interaction of subducted slabs with the mantle transition-zone: A regime diagram from 2-D thermo-mechanical models with a mobile trench and an overriding plate. *Geochem., Geophy., Geosy.,* **15,** 739-1765 (2014).

52. Katz, R.F., Spiegelman, M. and Langmuir, C.H. A new parameterization of hydrous mantle melting. *Geochemistry, Geophysics, Geosystems*, **4,** (2003).

53. Duvernay, T., Davies, D.R., Mathews, C.R., Gibson, A.H. and Kramer, S.C. Continental Magmatism: The Surface Manifestation of Dynamic Interactions Between Cratonic Lithosphere, Mantle Plumes and Edge-Driven Convection. *Geochemistry, Geophysics, Geosystems*, **23,** (2022).

54. Kohlstedt, D. L., Evans, B. & Mackwell, S. J. Strength of the lithosphere: constraints imposed by laboratory experiments. *J. Geophys. Res.*, **100,** 17587–17602 (1995).

55. Bischoff, S.H., Flesch, L.M. Normal faulting and viscous buckling in the Tibetan Plateau induced by a weak lower crust. *Nat Commun.*, **9,** 4952 (2018).

56. Stixrude, L. & Lithgow-Bertelloni, C. Mineralogy and elasticity of the oceanic upper mantle: origin of the low-velocity zone, *J. Geophys. Res.,* **110** (2005).

57. Stixrude, L. & Lithgow-Bertelloni, C. Thermodynamics of mantle minerals - II. Phase equilibria, *J. Geophys. Int.*, **184,** 1180–1213 (2011).

58. Cammarano, F., Goes, S., Deuss, A. & Giardini, D. Is a pyrolitic adiabatic mantle compatible with seismic data? *Earth Planet. Sci. Lett.*, **232,** 227–243 (2005).

59. Connolly, J. Computation of phase equilibria by linear programming: a tool for geodynamic modeling and its application to subduction zone decarbonation, *Earth Planet. Sci. Lett.*, **236,** 524–541 (2005).

60. Le Voci, G., Davies, D. R., Goes, S., Kramer, S. C., & Wilson, C. R. A systematic 2-D investigation into the mantle wedge's transient flow regime and thermal structure: Complexities arising from a hydrated rheology and thermal buoyancy. *Geochem. Geophys. Geosyst*, **15,** 28-51 (2014).

Correspondence and requests for material should be addressed to S.P. (simone.pilia@kfupm.edu.sa).